The optimum fire window: applying the fire-productivity hypothesis to Jurassic climate states

Teuntje P. Hollaar*[1,2], Claire M. Belcher[1], Micha Ruhl[3], Jean-François Deconinck[4], Stephen P. Hesselbo[2,5]

[1]WildFIRE Lab, Global Systems Institute, University of Exeter, Exeter, EX4 4PS, UK

[2]Camborne School of Mines, Department of Earth and Environmental Sciences, University of Exeter, Penryn Campus, Penryn, TR10 9FE, UK

[3]Department of Geology, Trinity College Dublin, The University of Dublin, College Green, Dublin, Ireland

[4]Biogéosciences, UMR 6282 CNRS, Université de Bourgogne/Franche-Comté, 21000 Dijon, France

[5]Environment and Sustainability Institute, University of Exeter, Penryn Campus, Penryn, TR10 9FE, UK

*Corresponding author: t.p.hollaar@uu.nl

Abstract

Present day fire frequency has been suggested to relate to a productivity/aridity gradient on a regional and global scale. Optimum fire conditions occur at times of intermediate productivity and aridity, whereas fire is limited on the high productivity (moisture) and aridity (no fuel) endmembers. However, the current global fire activity pattern is biased by the predominant burning of grasslands. Here we test the intermediate fire-productivity hypothesis for a time period on Earth before the evolution of grasses, the Early Jurassic, and explore the fire regime of two contrasting climatic states: the Late Pliensbachian (LPE) cooling Event and the Sinemurian – Pliensbachian Boundary (SPB) warming. Palaeo-fire records are reconstructed from fossil charcoal abundance, and changes in the hydrological cycle are tracked via clay mineralogy, which allows inference of changes in fuel moisture status. Large fluctuations in the fossil charcoal on an orbital eccentricity time scale indicate two modes of fire regime at the time. Wildfires were moisture limited in a high productivity ecosystem during eccentricity minima for both the SPB and LPE. During eccentricity maxima, fires increased, and an optimum fire window was reached, in which heightened seasonality led to intermediate states of productivity and aridity. The LPE experienced more extreme climatic endmembers compared to the SPB, with the fire regime edging closer to 'moisture limitation' during

34 eccentricity minima, and more pronounced seasonality during eccentricity maxima, explained by the

35 overall cooler climate at the time. This study illustrates that the intermediate-productivity gradient

36 holds up during two contrasting climatic states in the Jurassic.

37

38 **Plain Language Summary**

39 Fires are limited in year-round wet climates (tropical rainforests, too wet), and in year-round dry

40 climates (deserts, no fuel). This concept, the intermediate-productivity gradient, explains the global

41 pattern of fire activity. Here we test this concept for climate states of the Jurassic (~190 Myr ago). We

42 find that the intermediate-productivity gradient also applies in the Jurassic, despite the very different

43 ecosystem assemblages, with fires most frequent at times of high seasonality.

44

45 **Key Points**

46 • The intermediate-fire productivity gradient can be applied to the Jurassic and be utilized to

47 explain shifts in biomass, rainfall and fire.

48 • The terrestrial ecosystem surrounding the Cardigan Bay Basin was not year-round dry during

49 the Sinemurian–Pliensbachian Boundary warming Event or the Late Pliensbachian Cooling

50 Event and therefore fire was not aridity limited.

51 • Fire activity was strongly influenced by the ~100 kyr and 405 kyr eccentricity cycle during

52 both climatic states, which led to two modes in the fire regime: productivity limited (minima)

53 and the optimum fire-window (maxima).

54

55

56

57

58

59

60

61

62

1 Introduction

The global distribution of fire at the present day follows the intermediate-productivity concept. This concept states that fire activity increases non-linearly along a productivity gradient primarily controlled by biomass and fuel availability (Pausas & Bradstock, 2007; Pausas & Ribeiro, 2013). Climate drives fuel availability, structure, and moisture, which are the main ingredients of the fire regime. Fire is either limited by high moisture and biomass production, for example in tropical rainforests, or in high aridity and low biomass production ecosystems, such as deserts. This principle explains drought-driven fire regimes and fuel-limited fire regimes (Pausas & Ribeiro, 2013). In humid regions fires are initiated because aridity leads to flammable conditions and lower fuel-moisture status. In unproductive arid regions it is biomass production that determines fire activity, as the fuel-moisture status would not be limiting (Pausas & Ribeiro, 2013). The optimum window for wildfires is at intermediate productivity levels, such as tropical savannahs, wherein biomass can accumulate due to seasonal precipitation and fuel becomes available in the dry season when the fuel moisture status lowers (Meyn et al., 2007; Pausas & Bradstock, 2007; Krawchuk & Moritz, 2011; Pausas & Paula, 2012; Pausas & Ribeiro, 2013).

The intermediate-productivity concept provides an effective explanation for the distribution of fire on a global and regional scale where highest fire activity is found at intermediate moisture availability (Meyn et al., 2007; Krawchuk & Moritz, 2011; Daniau et al., 2012). However, the observation of high fire activity in ecosystems that are of intermediate aridity and productivity is strongly driven by grass biomes (Archibald et al., 2018). In the present day, >80 % of area burnt is grasslands (van der Werf et al., 2006), thus this vegetation group clearly biases these generalisations (Archibald et al., 2018). Since fire has formed an important part of ecosystems and the Earth system since 420 Ma (Glasspool et al., 2004; Glasspool & Gastaldo, 2022), we therefore ask how long the intermediate-productivity gradient has existed and if the concept also applied in a world before the evolution of grasses.

Here we look back at two contrasting climate events in the Early Jurassic, ~190 Myr ago, to assess what evidence there is for the existence of the intermediate-productivity fire gradient at such time (Fig. 1). The first event, the Sinemurian-Pliensbachian Boundary event (SPB, is marked by global warming, sea-level rise, increased humidity, and a negative carbon-isotope excursion (Ruhl et al., 2016; Haq, 2018; Deconinck et al., 2019; Storm et al., 2020). In contrast, the second event, the late Pliensbachian Event (LPE) is marked by ~5 °C cooling in NW Europe, greater aridity, sea-level fall and a global positive carbon-isotope excursion (e.g. Korte et al., 2015; Ruhl et al., 2016; Haq, 2018; Deconinck et al., 2019; Storm et al., 2020). We couple charcoal, clay and climate data to infer palaeo-fire and the hydrological regimes during both these time intervals.

2 Materials and Methods

Materials

The records from both time periods are taken from the Llanbedr (Mochras Farm) borehole, from sedimentary strata deposited in a relatively deep marine setting close to the shore in the Cardigan Bay Basin (Wales, UK). These sediments show a strong regular orbital control in the limestone-mudstone alternations (Ruhl et al., 2016), and an existing astrochronological framework allows for time constraints. In addition, input of terrestrial organic matter input in the sampled section is relatively high (van de Schootbrugge et al., 2005; Riding et al., 2013), and thus provides ideal material to study palaeo-fire regimes with a high temporal constraint.
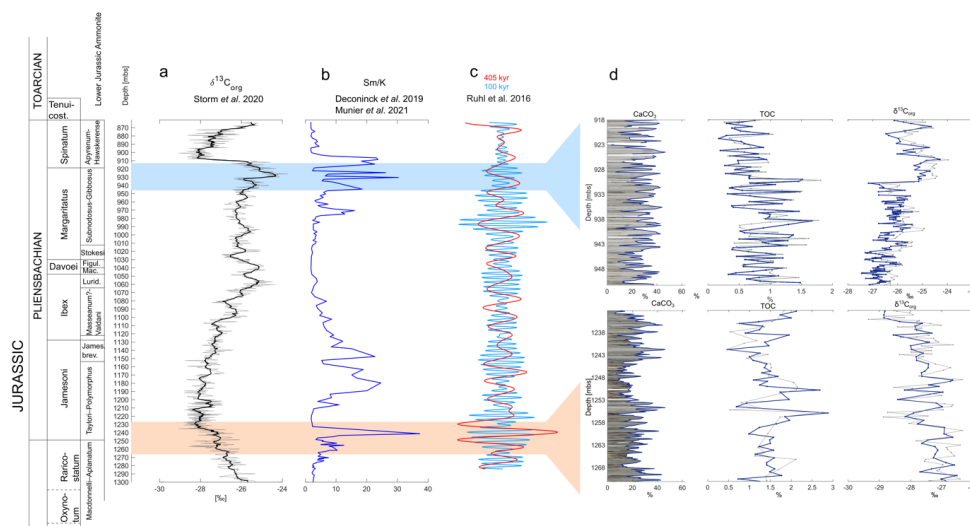
Fig. 1: *Cyclostratigraphic framework of the latest Sinemurian–Pliensbachian of the Mochras core and the two intervals here studied. Red bar represents the interval (1271–1233 mbs) of the SPB and the blue bar represents the interval of the LPE (951–918 mbs) (a) The $\delta^{13}C_{org}$ record from the Mochras core (Storm et al., 2020), shows the broad negative carbon-isotope trend around the SPB and the positive carbon-isotope excursion (CIE) in the Late Pliensbachian. (b) The smectite/kaolinite (Sm/K) ratio reflects changes in the hydrological cycle; data from Deconinck et al. (2019) and Munier et al. (2021). Peaks in smectite indicate greater climatic aridity (Deconinck et al., 2019; Munier et al., 2021). (c) Orbital filters of the 100 kyr and 405 kyr cycle based on the Ca and Ti elemental records in the depth domain from Ruhl et al. (2016). (d) The LPE interval is carbonate-rich and shows the metre-scale variations in $CaCO_3$ and TOC, next to the $\delta^{13}C_{org}$ positive shifts that marks the onset of the LPE. (e) The SPB interval contains relatively more clay and lithological couplets of alternating $CaCO_3$ and TOC-enhanced beds occurring on a metre scale. The $\delta^{13}C_{org}$ shows the negative trend of the long-negative limb of the SPB negative CIE.*

122   The Mochras core was drilled between 1967 and 1969 on the coast in NW Wales, UK. Preserved 1-m-

123   length core slabs of the core are stored at the British Geological Survey National Core Repository at

124   Keyworth, United Kingdom. The Pliensbachian of Mochras shows alternating beds of pale grey

125   limestone and dark brown to grey mudstone (Ruhl et al., 2016). These couplets occur throughout the

126   Pliensbachian, but vary in thickness, from about 90 cm at the Sinemurian–Pliensbachian boundary to

127   about 30 cm in the Late Pliensbachian age strata (latest Margaritatus and Spinatum zones) (Ruhl et al.,

128   2016). The lithological couplets are well expressed around the SPB and in the Margaritatus Zone

129   (Ruhl et al., 2016). For this study, samples were taken at an average sample spacing of 90 cm across

130   the Sinemurian–Pliensbachian boundary (1272–1233 mbs (metres below surface)). In addition, data

131   are utilized in this study that are published in Hollaar et al. (2021; 2023), from the Late Pliensbachian

132   interval that is sampled at a 10 cm (951–934 mbs) and 30 cm (934–918 mbs) resolutions. The

133   macrocharcoal data between 934–918 mbs are new and not previously published.

134   *Palaeolocation*

135   During the Early Jurassic, the Mochras site was situated in the Boreal realm of the Laurasian Seaway,

136   which contained an island archipelago, and covers most of present-day NW and W Europe. The

137   Mochras site was situated at a palaeolatitude of ~ 35° N (Torsvik & Cocks, 2017), just off the Welsh

138   Massif, in a relatively deep marine setting, below storm base (Pieńkowski et al., 2021), but with a

139   strong terrestrial influence (van de Schootbrugge et al., 2005; Riding et al., 2013; Xu et al., 2018;

140   Storm et al., 2020).

141   *Methods*

142   Mass spectrometry $\delta^{13}C_{org}$, TOC and CaCO$_3$

143   Bulk organic carbon-isotopes, TOC and carbonate content were measured to track changes in the

144   carbon-cycle and changes in total organic matter in the studied interval. For the SPB interval (1271–

145   1233 mbs) 50 samples and for the LPE (934–918 mbs) 43 samples were processed for carbon isotope

146   mass spectrometry. Bulk rock samples were powdered using a pestle-a-mortar, weighed into

147   centrifuge tubes, and decarbonated using 3.3 % HCl. Following, the samples were transferred to a hot

148   bath (79 °C) for 1 h to remove siderite and dolomite. After this, the samples were centrifuged and the

149   liquid decanted, this step repeated until the samples were neutralized (on average 2 times). Finally, the

150   samples were oven-dried, re-powdered, and weighed (to measure CaCO$_3$ loss) and transferred into

151   small tin capsules for mass spectrometry (TOC and $\delta^{13}C_{org}$), at the University of Exeter, Penryn

152   Campus.

153   Charcoal quantification and palynofacies

154   For the SPB interval, 54 samples were prepared for charcoal analysis and 42 for palynofacies at the

155   University of Exeter, Streatham Campus. For the LPE interval, an additional 50 macrocharcoal

156   samples were analysed, to compliment a total of 204 macrocharcoal samples for this interval. A total

157   of 162 samples for palynofacies and 200 microcharcoal samples are included in the LPE study

158   interval.

159   Rock samples of 10–30 g weight were split into 0.5 cm^3 fragments to minimize the breakage of the

160   organic particles whilst optimizing the surface area for palynological acid maceration. First, the 190

161   samples were treated with 10 % and 37 % HCl to remove carbonate. After this, hydrofluoric acid (40

162   % HF) was added to remove silicates from the sample. The samples were left to digest for 48 h, after

163   which cold concentrated HCl (37 %) was added to avoid calcium fluoride precipitation. Each sample

164   was left to settle, after which it could be decanted and topped up with DI water, a step that was

165   repeated ~ 6 times in order for the sample to neutralize.

166   After neutralizing, 5 droplets of the mixed residue were taken for the analysis of palynofacies (total

167   particulate organic matter) prior to any sieving. The remaining residue was sieved through a 125 µm

168   sieve and a 10 µm sieve to retrieve the macroscopic fraction (> 125 µm) and microscopic fraction

169   (10–125 µm). Macroscopic charcoal (>125 µm) was quantified using a Zeiss Stemi microscope, with

170   a 10 x 4 magnification lens and top lighting from a 'goose necked' light source. The entire

171   macroscopic fraction was dispersed in a Petri dish filled with DI water and the number of charcoal

172   particles counted and expressed per 10 g of processed rock (n/g). In some samples large clusters of

173   matrix were not digested by the acid, in which case they were taken out and dry weighed to deduce

174   the weight of the total processed rock.

175   Microscopic charcoal (10–125 µm) was analysed on a palynological slide. A known quantity of 125

176   µl of the microscopic fraction was mounted onto microscopic slides using glycerine jelly. A

177   transmitted light microscope (Olympus (BX53)) with a 40 x 10 magnification was used to count the

178   charcoal particles. Four transects per slide were counted, one transect on the left, two in the middle,

179   and one on the right of the coverslip. These data were then scaled up to the known quantity of the total

180   sample (Belcher et al., 2005). Palynofacies were examined to record shifts in the type of organic

181   matter (terrestrial vs marine) and potential changes in organic matter preservation and/or terrestrial

182   runoff. Palynofacies were quantified using the optical light microscope and a minimum of 300 organic

183   particles per palynological slide was counted. The types of organic matter were roughly grouped after

184   Oboh-Ikuenobe et al. (2005): terrestrial palynomorphs (spores and pollen), marine palynomorphs

185   (dinoflagellates, acritarchs, prasinophytes and foraminifera test linings), fungal remains, structured

186   phytoclasts (wood particles, parenchyma), unstructured phytoclasts (degraded plant remains),

187   charcoal, black debris (palynomorphs filled with pyrite) and amorphous organic matter (AOM: fluffy,

188   clotted and granular masses, colour ranging between almost colourless to yellow and pale brown).

189   XRD clay mineralogy

190   A total of 55 samples were prepared for clay mineralogy spanning the SPB interval. About 5 g of

191   bulk-rock sample was gently crushed and powdered with an agate mortar, after which about 2–3 g of

192   the powdered sample was decarbonated with a 0.2 M HCl solution. The samples were left to settle for

193   95 min, after which the suspended clay sized fraction (< 2 µm) was extracted with a syringe following

194   Stokes law. The clay fraction was centrifuged and subsequently smeared and oriented on glass slides.

195   The samples were analysed by X-ray diffraction (XRD) using a Bruker D4 Endeavour diffractometer

196   (Bruker, Billerica, MA, USA) with Cu Kα radiations, LynxEye detector and Ni filter under 40 kV

197   voltage and 25 mA intensity at the Biogéosciences Laboratory, Université Bourgogne/FrancheComté,

198   Dijon. Three runs were performed per sample to discriminate the clay phases: (1) air-drying at room

199   temperature; (2) ethylene-glycol solvation for 24 h; (3) heating at 490 °C for 2 h, following Moore &

200   Reynolds (1997). Comparing the three diffractograms obtained, the clay minerals were identified

201   using their main diffraction (d0001) peak. The proportions of each clay mineral on glycolated

202   diffractograms was estimated with the MACDIFF 4.2.5 software (Petschick, 2000). The identification

203   of the clay minerals further follows the methods in Moore & Reynolds (1997) and Deconinck et al.

204   (2019).

205   Orbital filters and the charcoal record

206   The Pliensbachian of the Mochras core has a well-established astrochronological framework (Ruhl et

207   al., 2016; Hinnov et al., 2018; Storm et al., 2020; Hollaar et al., 2021; Pienkowski et al., 2021). Based

208   on the existing cyclostratigraphy, the 100 kyr eccentricity cycle lies within the range of 3.2–10.2 m

209   (Ruhl et al., 2016; Hinnov et al., 2018), 6.3–4.8 m (Storm et al., 2020), and ~5.3 m (Pieńkowski et al.,

210   2021) for the studied intervals. The here studied intervals of the SPB and LPE compromise ~8–9 short

211   eccentricity cycles. No spectral analysis has been performed on the records presented here because of

212   the limited time span represented. Instead, we compare the charcoal and clay records visually with the

213   100 kyr and 405 kyr filters based on Ca and Ti (Ruhl et al., 2016; Hinnov et al., 2018).

214

215   **3 Results**

216   The data presented here that cover the run-up to and onset of the SPB (1271–1233 mbs) show a ~1.8

217   ‰ negative shift in $\delta^{13}C_{org}$ spanning the end of the negative CIE limb in the Mochras borehole and

218   reaching most negative values. The results of the LPE interval which encompass the run-up and onset

219   of the LPE (951 – 918 mbs), show a rapid positive shift in the $\delta^{13}C_{org}$ of ~1.8 ‰ (between 930.8 –

220   930.4 mbs) (in agreement with Storm et al., 2020).

221   Large fluctuations are observed in the abundance of both macroscopic (>125 µm) and microscopic

222   (10–125 µm) fossil charcoal for both CIEs. For the SPB, microcharcoal abundance fluctuates from

223   $2x10^4$–$4.2x10^5$ (mean $2x10^5$) particles per 10 g of sediment, and the number of macrocharcoal

224   particles varies from 99–2327 (mean 787) particles per 10 g sediment (Fig. 2). A similar trend is

225   observed in both size fractions, with individual charcoal peaks fluctuating on a 2–4 m scale (Fig. 2).

226   In the higher resolution LPE interval, metre-scale individual peaks of charcoal abundance are

227   observed, with microcharcoal abundance fluctuating from 4.5×10^3–4.3×10^5 (mean 1.1×10^5) particles

228   per 10 g of sediment, and the number of macrocharcoal particles varies from 8–2276 (mean 376)

229   particles per 10 g sediment (Fig. 3). Longer term fluctuations in the macrocharcoal record are also

230   observed, with bundling of peaks visible every ~4–5 m. Micro- and macro-charcoal are more

231   abundant in the SPB compared to the LPE (Fig. 4).

232
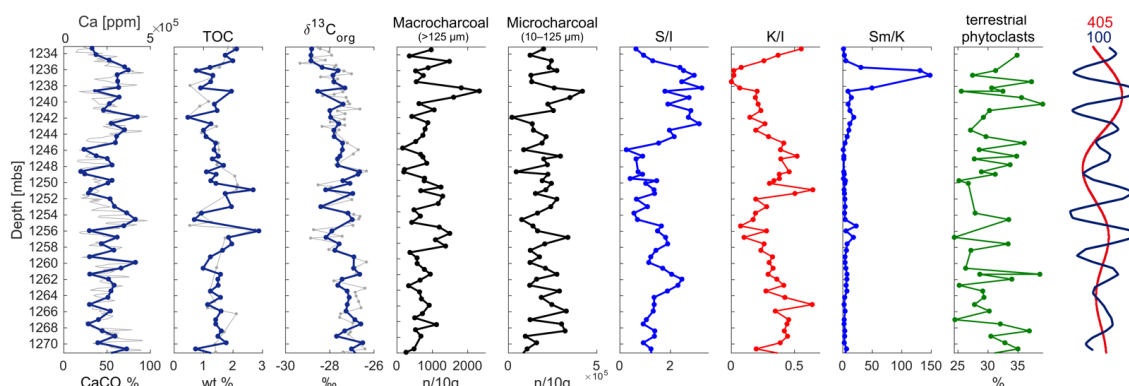
233   **Fig. 2:** *The SPB studied interval showing all proxies of this study in context of the orbital filters*

234   *(Ruhl et al., 2016). The CaCO₃, TOC and $\delta^{13}C_{org}$ (blue) data obtained for the present study are*

235   *plotted over previously published data (light grey – Ruhl et al., 2016; Storm et al., 2020). The*

236   *macrocharcoal abundance shows ~5 peaks throughout the studied interval. The majority of*

237   *macrocharcoal peaks are mirrored in the microcharcoal fraction. Alternating phases of increase in the*

238   *smectite/illite ratio (S/I) and the kaolinite/illite ratio (K/I) indicate swings in the hydrological cycle.*

239   *This is further indicated by the smectite/kaolinite ratio (Sm/K). The percentage of terrestrial*

240   *phytoclasts shows that the terrestrially sourced organic particles fluctuate around 30% in the studied*

241   *interval. Finally, the orbital filters of Ruhl et al. (2016) indicate that the clay records shift dominance*

242   *on a 405 kyr time scale. The peaks in the macrocharcoal record occur on a 100 kyr time scale.*

243
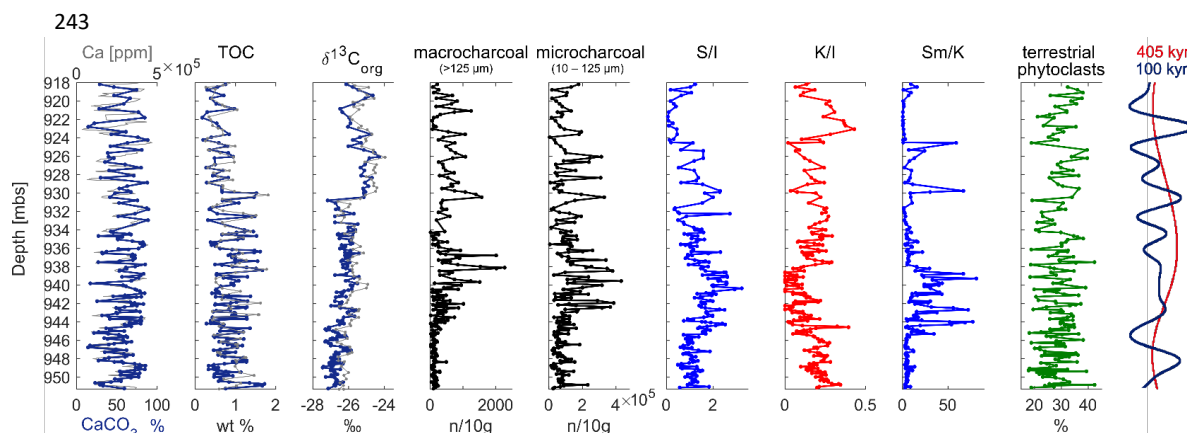
Fig. 3: Synthesis of the LPE interval showing all proxies considered in this study in context of the

orbital filters (Ruhl et al., 2016). *The CaCO₃, TOC and δ¹³C_org (blue) from Hollaar et al. (2023) are*

plotted over independently generated data (light grey - Ruhl et al., 2016; Storm et al., 2020). The

macrocharcoal abundance shows ~5 peaks throughout the studied interval. The majority of

macrocharcoal peaks are mirrored in the microcharcoal fraction. Alternating phases of increase in the

smectite/illite ratio (S/I) and the kaolinite/illite ratio (K/I) indicate swings in the hydrological cycle.

This is further indicated by the smectite/kaolinite ratio (Sm/K). The percentage of terrestrial

phytoclasts shows that the terrestrially sourced organic particles fluctuate around 30 % in the studied

interval. Finally, the orbital filters of Ruhl et al. (2016) are placed next to the proxy records. This

shows that the clay records shift dominance on a 405 kyr time scale. The peaks in the macrocharcoal

record occur on a 100 kyr time scale.

The palynofacies of both intervals is typically marine (AOM>58%). The proportion of terrestrial vs

marine organic matter remains relatively stable through both the SPB and LPE, varying between 24.4

and 39.1% (mean 30.7%), and 17.7 and 42.3% (mean 28.9%), respectively. Charcoal accounts for

~3.7% and ~4.5% of the total particulate organic matter, respectively for the SPB and the LPE

intervals (SI Fig. 1). The abundance of macrocharcoal is not influenced by the percentage of terrestrial

particulate organic matter through the SPB and LPE intervals (SPB r = -0.12, p = 0.42; LPE r = 0.06,

p = 0.46) and nor is the microcharcoal abundance for the SPB interval (r = 0.07, p = 0.62). However, a

very weak correlation exists between the percentage of terrestrial phytoclasts and microcharcoal

abundance in the LPE interval (r = 0.16, p = 0.05). These results suggest that the preservation and/or

influx of terrestrial particulate organic matter is not the main driver of fluctuations in charcoal
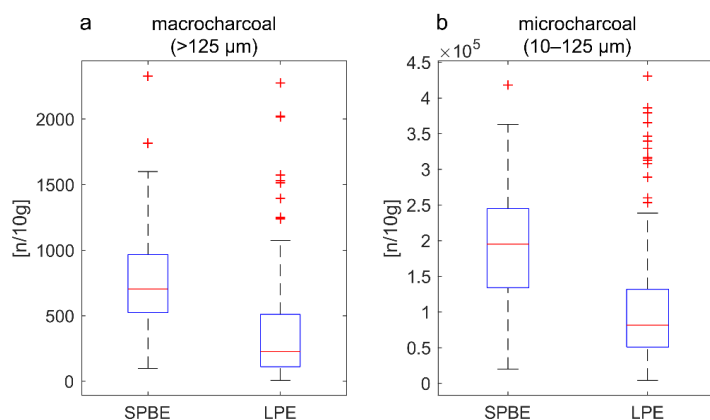
abundance.

Fig. 4: *Distribution boxplots of the macrocharcoal and microcharcoal abundance of the SPB and LPE studied intervals. (a) Average macrocharcoal abundance is higher in the SPB interval compared to the LPE interval, however, the absolute minimum and maximum are similar. (b) Average microcharcoal abundance is higher for the SPB compared to the LPE. The minimum number of microcharcoal particles is lower for the LPE, however, the maximum microcharcoal abundance is similar in both records.*

The clay mineral assemblages of the SPB and LPE are dominated by illite, kaolinite and smectite (I-S R0), with smectite increasing in parallel with decreases of illite and kaolinite (SI Fig. 2). Low proportions of chlorite and sparse I-S R1 are present in the SPB record. Chlorite and I-S R1 are generally low in the LPE record but increase between 924–219 mbs (SI Fig. 2). Two smectite-enhanced phases occur for the SPB, at 1264–1255 mbs and 1245–1235 mbs. Both these phases are coeval with high charcoal abundance (both size fractions) (Fig. 2). Additionally, the LPE interval encompasses two stratigraphic intervals rich in smectite; from 944–937 mbs and 931–924 mbs. Charcoal abundance (both size fractions) increases overall, and coevally with the S/I, over ~ 5 m scale fluctuations, and decreases at levels with high K/I (Fig. 3). The 3.2–10.2 m orbital filter of the macrocharcoal records (interpreted as the 100 kyr eccentricity (Ruhl et al., 2016; Hinnov et al., 2018; Storm et al., 2020; Pienkowski et al., 2021)), indicates that the observed fluctuations in the macrocharcoal record occur with a 100 kyr periodicity (SI Fig. 6).

4 Discussion

Charcoal transport and preservation

The charcoal records for both the SPB and LPE intervals do not appear to be linked to the terrestrial

291 influx of materials, as evidenced by the palynofacies. No parallel trends are observed between the

292 abundance of terrestrial phytoclasts and the number of charcoal particles, which suggests that the

293 abundance of charcoal is not a reflection of preservation and/or runoff changes. Inferred sea level

294 changes during the LPE and the SPB could potentially have impacted the charcoal abundance record

295 and the clay mineralogy. Transgression and relative sea-level rise during the SPB has been extensively

296 recorded from the Boreal and Tethys regions, and from South America (e.g. Legarreta and Uliana,

297 1996; de Graciansky et al., 1998; Hesselbo & Jenkyns, 1998; Danisch et al., 2019; Silva et al., 2021).

298 The Late Pliensbachian is characterized by widespread regressive facies and inferred relative sea-level

299 fall, likely indicating a closer proximity to shore also in the Mochras borehole. Fossil wood in the

300 Mochras borehole has been shown to become more abundant at this time, suggesting a potential bias

301 of higher terrestrial input from a nearby landmass (Ullmann et al., 2022). However, the mean

302 abundance of macrocharcoal and microcharcoal is higher during the SPB (mean of 787 and 2×10^5

303 respectively) compared to the LPE (mean of 376 and 1.1×10^5 respectively) in the Mochras borehole,

304 suggesting that the shore proximity did not impact overall charcoal abundance. Similarly, the

305 palynofacies analysis indicates that the mean abundance of terrestrial particulate organic matter during

306 the SPB (30.7%) is not higher compared to the LPE (28.9%). Hence, we take this as strong evidence

307 that the record of fossil charcoal records changes in wildfire activity.

308 *Orbital forcing of the hydrological cycle and fire*

309 Alternations in the dominance of smectite and kaolinite occur approximately every 10 m in both the

310 LPE and SPB records. Kaolinite and smectite reflect hydrological changes in the palaeoenvironment

311 of the Cardigan Bay Basin (Deconinck et al., 2019; Munier et al., 2021). As the smectite and kaolinite

312 clay minerals are detrital in character and their abundance varies in opposition to one another (Fig. 2

313 and 3), these clays are likely derived from pedogenic weathering profiles (Deconinck et al., 2019).

314 Smectite preferentially forms under a hot and seasonally arid climate, similar to a monsoonal climate

315 system or the winter-wet climate of the Mediterranean zone (Chamley, 1989; Deconinck et al., 2019).

316 Kaolinite is indicative of an accelerated hydrological cycle, increased runoff and a year-round wet

317 climate (Chamley, 1989; Ruffell et al., 2002) either via formation in strong weathering profiles or via

318 the physical erosion of kaolinite-bearing rocks (Chamley, 1989). At times of high smectite abundance,

319 fire activity is greatest as observed from the macro- and micro-scopic charcoal fractions (Fig. 2 and

320 3). Based on the astrochronological framework of the Mochras borehole (Ruhl et al., 2016; Hinnov et

321 al., 2018; Storm et al., 2020; Pieńkowski et al., 2021) these alternations appear to occur in concert

322 with the 405 kyr long-eccentricity cycles (Fig. 2, Fig. 3). Eccentricity modulates the precession driven

323 changes in seasonal and latitudinal distribution of insolation (Imbrie & Imbrie, 1980; Berger et al.,

324 1989). One ~20 kyr precession cycle can represent a strongly seasonal extreme climate for ~10 kyr

325 and a weakly seasonal climate for the subsequent ~10 kyr. The geological record averages the

326   amplification or suppression of seasonality between years (SI Fig. 4). Eccentricity forcing modulates

327   the amplitudes of these extremes in seasonality with periodicities of 100 kyr and 405 kyr.

328   In the Mesozoic, eccentricity maxima are commonly associated with dry climates that are disrupted

329   by short and intense periods of precipitation and storm activity in the boreal landmasses bordering the

330   NW Tethys (Martinez & Dera, 2015). In contrast, eccentricity minima are characterized by a more

331   moderate seasonal contrasts and year-round wet conditions (Martinez & Dera, 2015). Eccentricity

332   minima are linked to periods of enhanced runoff and weathering conditions as evidenced by high

333   kaolinite content, $^{87}Sr/^{86}Sr$, and negative shifts in $\delta^{18}O$ (Martinez & Dera, 2015). Therefore, we link

334   the observed smectite-rich intervals to eccentricity maxima and the kaolinite-rich intervals to

335   eccentricity minima. Charcoal abundance is highest during the seasonal climate of the eccentricity

336   maxima for the SPB, in agreement with the previous findings for the LPE (Hollaar et al., 2021, 2023).

337   Both the LPE and SPB study intervals span two 405-kyr cycles (Ruhl et al., 2016; Hinnov et al., 2018;

338   Storm et al., 2020; Pieńkowksi et al., 2021). The relative abundance of smectite and the abundance of

339   charcoal both reach a peak during the maxima in the long eccentricity cycle, supporting the notion

340   that orbitally driven changes in seasonal contrast led to high fire activity. Within these long-term

341   trends, the macrocharcoal record also shows ~ 5 m scale individual peaks or clusters in both the LPE

342   and SPB records (SI Fig. 3, Fig. 2 and 3). Based on the existing age model (Ruhl et al., 2016; Hinnov

343   et al., 2018; Storm et al., 2020; Pieńkowksi et al., 2021) we derive that this is the expression of the

344   ~100 kyr eccentricity cycle in the macrocharcoal record. The orbital filter representing the ~100 kyr

345   cycle in the Pliensbachian of the Mochras core, captures the observed ~5 m oscillations in the fire

346   record (SI Fig. 3, Fig. 2 and 3) (Ruhl et al., 2016; Hinnov et al., 2018; Storm et al., 2020; Pieńkowski

347   et al., 2021).

348   The Sinemurian–Pliensbachian transition is generally associated with an overall warm and humid

349   climate (Korte & Hesselbo, 2011; Gómez et al., 2016), and enhanced levels of runoff and weathering

350   (Bougeault et al., 2017). The results presented here suggest that within this overall warm and humid

351   background, orbital forcing created year-round wet periods, that were not conducive to frequent fire,

352   alternating with periods that remained warm but had a more seasonal climate, that allowed ignition

353   during the dry season. In contrast, the LPE, and the sediments of late Margaritatus ammonite

354   chronozone formed in an overall semi-arid climate with proposed lower runoff levels from the land

355   into the sea (Deconinck et al., 2019; Hollaar et al., 2021; 2023). During the run-up of the LPE we

356   infer orbitally forced alternating climatic states of more extreme seasonality (high fire and smectite)

357   and a more equitable year-round wet climate (low fire and high kaolinite) (Hollaar et al., 2021; 2023)

358   acting within this overall semi-arid climate phase. Overall, kaolinite fluctuates in abundance in

359   opposition to smectite, reflecting hydrological changes from wet and hot to semi-arid and hot, in

360   agreement with high fire activity during a seasonal climate and fire suppression during a year-round
361   wet climate for both the LPE and the SPB.

362   *Vegetation, fire and the intermediate fire-productivity gradient*
363   Fuel (vegetation biomass) and moisture status of the fuel, as governed by seasonal patterns in
364   precipitation and temperature, are major factors influencing fire regime and fire behaviour (Archibald
365   et al., 2009; Cochrane & Ryan, 2009; Bradstock, 2010; Archibald et al., 2013; Bowman et al., 2014;
366   Archibald et al., 2018). Ecosystems with low wildfire activity are generally associated with either
367   high precipitation and abundant primary productivity, or low productivity under strongly arid
368   conditions (Pausas & Paula, 2012). In contrast, high wildfire activity occurs in climates that are in the
369   middle of the productivity gradient, where biomass builds up enough to form a connected fuel
370   structure, and a period of drought allows the fuel to lose moisture content, which allows fire ignition
371   and more rapid spread (Pausas & Paula, 2012). The observed alternating modes of high and low fire
372   activity, as inferred from the lower Jurassic fossil charcoal record, during the onset of the SPB and
373   LPE, likely indicates shifts in seasonality of the Cardigan Bay Basin hinterland and would place both
374   the LPE and the SPB at intermediate productivity levels during maximum eccentricity forcing. The
375   intermediate fire-productivity hypothesis (Pausas & Bradstock, 2007; Pausas & Ribeiro, 2013)
376   conceptualizes this relationship between climate-vegetation-fire, where fire activity is plotted along an
377   aridity and productivity gradient. On the one extreme, in warm and wet climates fuel is abundant and
378   the fuel structure has a high degree of connectivity, but the high fuel moisture levels limit fire activity
379   (Fig. 5). In contrast, in an arid region, fuel would be sparse and fuel connectivity would be poor
380   limiting fire activity. Although the fuel moisture levels are low and make the fuel that is present
381   flammable, fire is unable to easily spread. Additionally, there is a higher sensitivity to fuel moisture
382   levels in the tropical or mesic areas, where a small fall in fuel moisture content can lead to more
383   flammable conditions (Cochrane, 2003). The deep time combined fire and hydrological records we
384   present here are in agreement with the intermediate productivity hypothesis of Pausas & Bradstock
385   (2007), even with very different vegetation assemblages, e.g., a world without grasses. We suggest
386   that both the LPE and the SPB switched between a state of low fire (either limited by climatic aridity
387   or the presence and presence and connectivity of fuel) and a state of high fire during which seasonal
388   contrast is high and an ideal 'fire window' exists in which biomass built up during the wet season
389   after which a fire-prone season followed (Fig. 5).

390
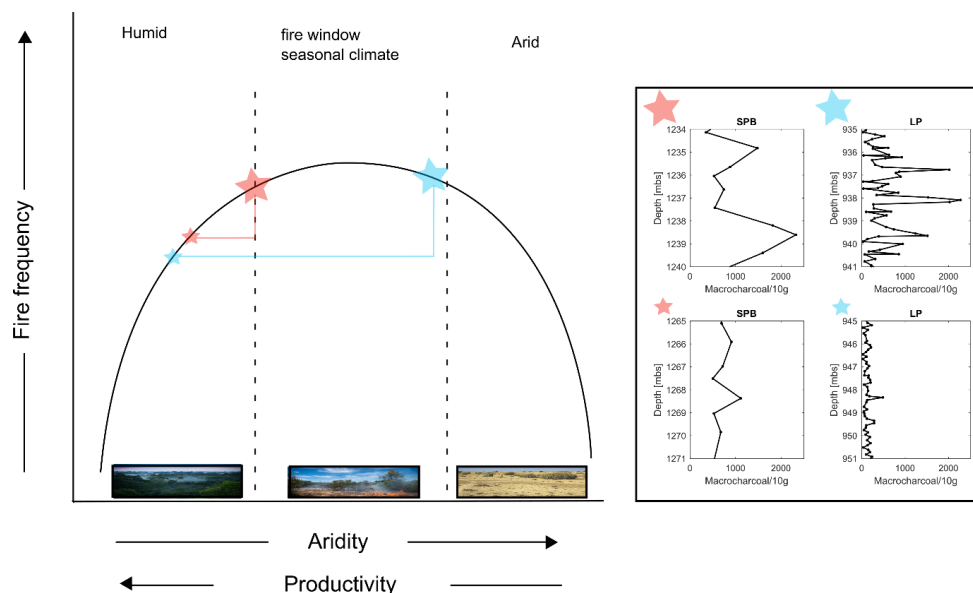
391 ***Fig. 5: The LPE and SPB fire records placed on the intermediate productivity gradient.*** *The graph*

392 *is adapted from Pausas & Bradstock (2007). Fire frequency is highest in the middle of the hyperbole,*

393 *medium levels of aridity and productivity created a seasonal climate in which seasonal biomass*

394 *growth was possible (productivity) and seasonally the fuel moisture limits were lower in a season of*

395 *drought (aridity), this created the optimized 'fire window'. The SPB is plotted on this fire-productivity*

396 *gradient in red: the small star indicates the eccentricity minimum state and the large star the*

397 *eccentricity maximum state. The LPE is plotted on the fire-productivity gradient in blue, and again the*

398 *small star indicates the eccentricity minimum and the large star the eccentricity maximum. The LPE*

399 *has a larger range compared to the SPB, and experienced more fire suppression due to high humidity*

400 *levels during eccentricity minima, and also was closer to a productivity limitation state during the*

401 *eccentricity maximum.*

402

403 Hence, in the more highly productive ecosystems fire activity is forced by the frequency of dry

404 weather/flammable conditions (Pausas & Paula, 2012). Low fire activity in the Lower Jurassic section

405 studied here is found to occur at times of high kaolinite/illite ratios, which indicates an enhanced

406 hydrological cycle, and likely a year-round wet climate.

407 We propose that the overall humid climate of the SPB fits the high productivity scenario, in which the

408 frequency of flammable conditions is the main factor controlling fire occurrences. Vegetation growth

409 likely occurred year-round in this warm and wet climate. No evidence was found to place the SPB on

410 the productivity-limiting high-aridity side of the fire gradient spectrum, where fire frequency would

have been mainly influenced by enhanced rainfall in an otherwise dry climate that would have
enabled biomass growth and fuel connectivity. These findings are in line with the presence of plant
cuticle through the studied interval, indicating the presence of vegetation during high and low modes
of fire activity. Hence, the SPB seems to conform to the humid and high productivity end of the
aridity gradient (Fig. 5 red lines). Within these constraints (Fig. 5) exists two states for the SPB; the
wetter end of the spectrum occurred during eccentricity minima (Fig. 5), and during eccentricity
maxima on each precession half-cycle conditions enter the seasonal side of the fire-productivity
gradient (towards aridity) to allow an increase in fire activity.

The fluctuations occurred over both long-eccentricity and short eccentricity timescales in the
macrocharcoal record showing longer phases of overall enhancement of fire (long-eccentricity) and
relatively abrupt shifts from low to high fire and back again (~100 kyr eccentricity). For this reason,
the SPB is placed on a steep portion of the fire-productivity gradient curve. Overall, the mean
charcoal abundance is relatively high, and no sustained periods of very low charcoal abundance are
observed in the SPB record, which indicates that the climate never became too wet to fully limit fire
activity at that time.

The Late Pliensbachian has been linked to a global cooling event, with a potential of 5–7 °C lowering
in temperature inferred for the NW Tethys region (Korte et al., 2015). The atmospheric moisture
holding capacity of a cooler climate is lower compared to a warm climate, in which a 1 °C cooling
likely lowers the water holding capacity of air by 7% (Trenberth et al., 2005). The presence of
terrestrial phytoclasts throughout confirms the presence of vegetation in the surrounding landmasses
throughout this period. The mean abundance of charcoal for the LPE section is slightly lower than that
of the SPB and the lowest charcoal abundances are coeval with a K/I enhancement, suggesting that
during eccentricity minima environmental conditions moved further into the humid zone of the fire-
productivity gradient (Fig. 5 blue line). Increasing eccentricity shifted the system to a more seasonal
climate where the fire and clay records indicate the presence of a wet season that allowed for build-up
of biomass followed by a dry season in which fire was able to be ignited and spread.

Conceptually, the relatively drier and cooler LPE climate would have resulted in conditions that are
more arid, shifting to the biomass-limited part of the productivity/ aridity – fire frequency gradient
during eccentricity maxima, compared to the SPB (Fig. 5 blue lines). This is supported by the large
fluctuations observed between low fire frequency and high fire frequency for the LPE and the fact that
estimated high fire periods did not occur suddenly, but rather were sustained over a larger part of the
cycle. Therefore, the phase of highest fire frequency operating in the seasonal 'fire window' as
indicated in figure 5 for the LPE (blue lines) likely occurred for a larger part of the fire productivity
gradient. Hence, conditions across the LPE occurred across a wider range of the productivity/aridity
spectrum of the fire frequency gradient (Fig. 5 blue lines) compared to the SPB. There is no evidence

446   that conditions ever became limited by aridity, and conditions during the LPE did not extend beyond

447   the seasonal fire window into the arid part of the productivity/aridity spectrum of the fire frequency

448   gradient.

449   Importantly, the Jurassic climate was overall warm and humid, about 5–10 °C warmer on global

450   average compared to today (e.g., Rees et al., 2000; Sellwood & Valdes, 2008), with ~ 3.5–10 times the

451   pre-industrial value of atmospheric pCO$_2$ during the Early Jurassic (e.g. Retallack, 2001; Beerling &

452   Royer, 2002; McElwain et al., 2005; Berner, 2006; Steinthorsdottir & Vajda, 2015; Li et al., 2020). In

453   this context, it may not be surprising that a relative cooling event in the Early Jurassic did not lead to

454   the aridity and biomass-limiting conditions observed during the last glacial, at latitudes of ~38 °C N

455   (Daniau et al., 2007).

5 Conclusions

457   The study of two different climatic 'background' states, at the LPE and the SPB, shows that fire

458   activity was strongly modulated by orbital eccentricity cycles. The 405 kyr shifts in the record of

459   wildfire prevalence reflect similar changes also in the hydrological cycle (based on clay mineralogy

460   data) showing that high fire activity occurred during periods of high seasonal contrast and that fire

461   activity was suppressed during periods of high year-round humidity, because the latter would have

462   enhanced the fuel moisture levels and prevented frequent ignition. The fire record of both climatic

463   events is limited by the high fuel moisture levels during eccentricity minima, but fires were more

464   prevalent during times of increased seasonality, every precession half-cycle during eccentricity

465   maxima. Hence, during both events fire activity was limited by the moisture content and not by the

466   productivity gradient. Both the SPB and the LPE climate systems were therefore situated on the

467   moisture-limited side of the intermediate fire-productivity gradient (Fig. 5). Due to the lower

468   moisture-holding capacity of cold air, the overall higher seasonality of the Late Pliensbachian and the

469   more sustained high fire-frequency periods (based on the charcoal record for the LPE) we place the

470   LPE towards the higher end of the aridity gradient, within maximum seasonality and maximum fire

471   frequency window of the fire productivity graph (Fig. 5). The SPB fire regime reflected a more humid

472   climate that shifted abruptly between low fire frequency to high fire frequency within less extreme

473   bounds on the aridity gradient. This research reveals that the intermediate-fire productivity hypothesis

474   (Pausas & Bradstock, 2007) can also be applied to high-resolution deep time records and that this

475   hypothesis explains well the influence of orbital cycles within different overall climate states, be they

476   cooling or warming trends. The coupling of high-resolution clay mineralogy and fossil charcoal

477   records, combined with constraints on orbital forcing at such time, allows for inferences on how

478   Earth's natural climate state variability has driven shifts in terrestrial productivity through the

479   geological past.

480 **Acknowledgements**

481 This is a contribution to the JET project funded by the Natural Environment Research Council

482 (NERC) (grant number NE/N018508/1). All authors acknowledge funding from the International

483 Continental Scientific Drilling Program (ICDP) and TPH acknowledges funding from the University

484 of Exeter.

485 **Conflict of Interest**

486 The authors declare no conflicts of interest relevant to this study.

487 **Data Availability Statement**

488 Supplementary data are available at the National Geoscience Data Centre at Keyworth (NGDC)

489 at https://doi.org/10.5285/1461dbe5-50a8-425c-8c49-ac1f04bcc271 (Hollaar, 2022) for the interval

490 934–918 m. b.s. All data presented for the interval 951–934 m. b.s. are available at the National

491 Geoscience Data Centre at Keyworth (NGDC) at https://doi.org/10.5285/d6b7c567-49f0-44c7-a94c-

492 e82fa17ff98e (Hollaar et al., 2021b). All data for the interval 1271–1233 mbs is deposited at the

493 University of Exeter: http://hdl.handle.net/10871/133255.

494 **Supporting Information**

495

496 **References**

497 Archibald, S., Lehmann, C. E., Belcher, C. M., Bond, W. J., Bradstock, R. A., Daniau, A. L., et al.

498 (2018). Biological and geophysical feedbacks with fire in the Earth system. *Environmental Research*

499 *Letters*, 13(3), 033003. https://doi.org/10.1088/1748-9326/aa9ead

500 Archibald, S., Lehmann, C. E., Gómez-Dans, J. L., & Bradstock, R. A. (2013). Defining pyromes and

501 global syndromes of fire regimes. *Proceedings of the National Academy of Sciences*, 110(16), 6442 –

502 6447. https://doi.org/10.1073/pnas.1211466110

503 Archibald, S., Roy, D. P., van Wilgen, B. W., & Scholes, R. J. (2009). What limits fire? An

504 examination of drivers of burnt area in Southern Africa. *Global Change Biology*, 15(3), 613 – 630.

505 https://doi.org/10.1111/j.1365-2486.2008.01754.x

506 Beerling, D. J., & Royer, D. L. (2002). Fossil plants as indicators of the Phanerozoic global carbon

507 cycle. *Annual Review of Earth and Planetary Sciences*, 30(1), 527 – 556.

508 https://doi.org/10.1146/annurev.earth.30.091201.141413

509 Belcher, C. M., Collinson, M. E., & Scott, A. C. (2005). Constraints on the thermal energy released

510 from the Chicxulub impactor: new evidence from multi-method charcoal analysis. *Journal of the*

511 *Geological Society*, 162(4), 591 – 602. https://doi.org/10.1144/0016-764904-104

512 Berger, A., Loutre, M. F. & Dehant, V. Astronomical frequencies for pre-Quaternary palaeoclimate

513 studies. *Terra Nova 1*, 474–479 (1989). https://doi.org/10.1111/j.1365-3121.1989.tb00413.x

514 Berner, R. A. (2006). GEOCARBSULF: a combined model for Phanerozoic atmospheric O2 and

515 CO2. *Geochimica et Cosmochimica Acta*, 70(23), 5653 – 5664.

516 https://doi.org/10.1016/j.gca.2005.11.032

517 Bougeault, C., Pellenard, P., Deconinck, J. F., Hesselbo, S. P., Dommergues, J. L., Bruneau, L., et al.

518 (2017). Climatic and palaeoceanographic changes during the Pliensbachian (Early Jurassic) inferred

519 from clay mineralogy and stable isotope (CO) geochemistry (NW Europe). *Global and Planetary*

520 *Change*, 149, 139 – 152. https://doi.org/10.1016/j.gloplacha.2017.01.005

521 Bowman, D. M., Murphy, B. P., Williamson, G. J., & Cochrane, M. A. (2014). Pyrogeographic

522 models, feedbacks and the future of global fire regimes. *Global Ecology and Biogeography*, 23(7),

523 821 – 824. https://doi.org/10.1111/geb.12180

524 Bradstock, R. A. (2010). A biogeographic model of fire regimes in Australia: current and future

525 implications. *Global Ecology and Biogeography*, 19(2), 145 – 158. https://doi.org/10.1111/j.1466-

526 8238.2009.00512.x

527 Chamley, H. (1989). *Clay Sedimentology*. Heidelberg: Springer Berlin Heidelberg.

528 Cochrane, M. A. (2003). Fire science for rainforests. *Nature*, 421(6926), 913 – 919.

529 https://doi.org/10.1038/nature01437

530 Cochrane, M. A., & Ryan, K. C. (2009). Fire and fire ecology: Concepts and principles. *Tropical fire*

531 *ecology*, 25 – 62. https://doi.org/10.1007/978-3-540-77381-8_2

532 Daniau, A. L., Bartlein, P. J., Harrison, S. P., Prentice, I. C., Brewer, S., Friedlingstein, P., et al.

533 (2012). Predictability of biomass burning in response to climate changes. Global Biogeochemical

534 Cycles, 26(4). https://doi.org/10.1029/2011GB004249

535 Daniau, A. L., Sánchez-Goñi, M. F., Beaufort, L., Laggoun-Défarge, F., Loutre, M. F., & Duprat, J.

536 (2007). Dansgaard–Oeschger climatic variability revealed by fire emissions in southwestern

537 Iberia. *Quaternary Science Reviews*, *26*(9-10), 1369 – 1383.

538 https://doi.org/10.1016/j.quascirev.2007.02.005

539 Danisch, J., Kabiri, L., Nutz, A., & Bodin, S. (2019). Chemostratigraphy of late Sinemurian–early

540 Pliensbachian shallow-to deep-water deposits of the Central High Atlas Basin: Paleoenvironmental

541 implications. *Journal of African Earth Sciences*, 153, 239 – 249.

542 https://doi.org/10.1016/j.jafrearsci.2019.03.003

543   Deconinck, J. F., Hesselbo, S. P., & Pellenard, P. (2019). Climatic and sea-level control of Jurassic

544   (Pliensbachian) clay mineral sedimentation in the Cardigan Bay Basin, Llanbedr (Mochras Farm)

545   borehole, Wales. *Sedimentology*, 66(7), 2769 – 2783. https://doi.org/10.1111/sed.12610

546   De Graciansky, P. C., Dardeau, G., Dommergues, J. L., Durlet, C., Marchand, D., Dumont, T., et al.

547   (1998). Ammonite biostratigraphic correlation and Early Jurassic sequence stratigraphy in France:

548   comparisons with some UK sections. In: de Graciansky, P.C., Hardenbol, J., Jacquin, T., Farley, M. &

549   Vail, P.R. (Eds.), Mesozoic and Cenozoic Sequence Statigraphy of European Basins. *Special*

550   *Publication of the Society for Sedimentary Geology (SEPM)*, 60, 583 – 622.

551   Glasspool, I. J., Edwards, D., & Axe, L. (2004). Charcoal in the Silurian as evidence for the earliest

552   wildfire. *Geology*, *32*(5), 381 – 383. https://doi.org/10.1130/G20363.1

553   Glasspool, I. J., & Gastaldo, R. A. (2022). Silurian wildfire proxies and atmospheric oxygen.

554   *Geology*. https://doi.org/10.1130/G50193.1

555   Gómez, J. J., Comas-Rengifo, M. J., & Goy, A. (2016). Palaeoclimatic oscillations in the

556   Pliensbachian (Early Jurassic) of the Asturian Basin (Northern Spain). *Climate of the Past*, 12(5),

557   1199 – 1214. https://doi.org/10.5194/cp-12-1199-2016

558   Haq, B. U. (2018). Jurassic sea-level variations: a reappraisal. *GSA today*, 28(1), 4 – 10.

559   https://doi.org/10.1130/GSATG359A.1

560   Hinnov, L. A., Ruhl, M. R., & Hesselbo, S. P. (2018). Reply to the Comment on "Astronomical

561   constraints on the duration of the Early Jurassic Pliensbachian Stage and global climatic fluctuations"

562   (Ruhl *et al*., (2016). *Earth and Planetary Science Letters*, 455, 149 – 165).

563   https://doi.org/10.1016/j.epsl.2017.10.061

564   Hesselbo, S.P. & Jenkyns, H.C. (1998). British Lower Jurassic sequence stratigraphy. In: de

565   Graciansky, P.C., Hardenbol, J., Jacquin, T., Farley, M. & Vail, P.R. (Eds.), Mesozoic–Cenozoic

566   Sequence Stratigraphy of European Basins. *Special Publication of the Society for Sedimentary*

567   *Geology (SEPM)*, 60, 561 – 581.

568   Hollaar, T. P., Baker, S. J., Hesselbo, S. P., Deconinck, J. F., Mander, L., Ruhl, M., & Belcher, C. M.

569   (2021). Wildfire activity enhanced during phases of maximum orbital eccentricity and precessional

570   forcing in the Early Jurassic. *Communications Earth & Environment*, 2(1), 1 – 12.

571   https://doi.org/10.1038/s43247-021-00307-3

572   Hollaar, T. P., Hesselbo, S. P., Deconinck, J. F., Damaschke, M., Ullmann, C. V., Jiang, M., &

573   Belcher, C. M. (2023). Environmental changes during the onset of the Late Pliensbachian Event

574   (Early Jurassic) in the Cardigan Bay Basin, Wales. Climate of the Past, 19(5), 979-997.

575   https://doi.org/10.5194/cp-19-979-2023

576 Imbrie, J., & Imbrie, J. Z. (1980). Modeling the climatic response to orbital variations. *Science*,

577 207(4434), 943 – 953. https://doi.org/10.1126/science.207.4434.943

578 Korte, C. & Hesselbo, S. P. (2011). Shallow marine carbon and oxygen isotope and elemental records

579 indicate icehouse-greenhouse cycles during the Early Jurassic. *Paleoceanography*, 26(4).

580 https://doi.org/10.1029/2011PA002160

581 Korte, C., Hesselbo, S. P., Ullmann, C. V., Dietl, G., Ruhl, M., Schweigert, G., & Thibault, N. (2015).

582 Jurassic climate mode governed by ocean gateway. *Nature communications*, 6(1), 1 – 7.

583 https://doi.org/10.1038/ncomms10015

584 Krawchuk, M. A., & Moritz, M. A. (2011). Constraints on global fire activity vary across a resource

585 gradient. *Ecology*, 92(1), 121 – 132. https://doi.org/10.1890/09-1843.1

586 Legarreta, L., & Uliana, M. A. (1996). The Jurassic succession in west-central Argentina: stratal

587 patterns, sequences and paleogeographic evolution. *Palaeogeography, Palaeoclimatology,*

588 *Palaeoecology*, 120(3-4), 303 – 330. https://doi.org/10.1016/0031-0182(95)00042-9

589 Li, X., Wang, J., Rasbury, T., Zhou, M., Wei, Z., & Zhang, C. (2020). Early Jurassic climate and

590 atmospheric CO 2 concentration in the Sichuan paleobasin, southwestern China. *Climate of the Past*,

591 16(6), 2055 – 2074. https://doi.org/10.5194/cp-16-2055-2020

592 Martinez, M. & Dera, G. (2015). Orbital pacing of carbon fluxes by a ∼ 9-My eccentricity cycle

593 during the Mesozoic. *Proceedings of the National Academy of Sciences*, 112, 12604 – 12609.

594 https://doi.org/10.1073/pnas.141994611

595 McElwain, J. C., Wade-Murphy, J., & Hesselbo, S. P. (2005). Changes in carbon dioxide during an

596 oceanic anoxic event linked to intrusion into Gondwana coals. *Nature*, 435(7041), 479 – 482.

597 https://doi.org/10.1038/nature03618

598 Meyn, A., White, P. S., Buhk, C., & Jentsch, A. (2007). Environmental drivers of large, infrequent

599 wildfires: the emerging conceptual model. *Progress in Physical Geography*, 31(3), 287 – 312.

600 https://doi.org/10.1177/0309133307079365

601 Moore, D. M. & Reynolds Jr, R. C. (1997). *X-ray Diffraction and the Identification and Analysis of*

602 *Clay Minerals*. Oxford: Oxford University Press.

603 Munier, T., Deconinck, J. F., Pellenard, P., Hesselbo, S. P., Riding, J. B., Ullmann, C. V., et al.

604 (2021). Million-year-scale alternation of warm–humid and semi-arid periods as a mid-latitude climate

605 mode in the Early Jurassic (late Sinemurian, Laurasian Seaway). *Climate of the Past*, 17(4), 1547 –

606 1566. https://doi.org/10.5194/cp-17-1547-2021

607 Oboh-Ikuenobe, F. E., Obi, C. G. & Jaramillo, C. A. (2005). Lithofacies, palynofacies, and sequence
608 stratigraphy of Palaeogene strata in Southeastern Nigeria. *Journal of African Earth Sciences*, 41, 79–
609 101. https://doi.org/10.1016/j.jafrearsci.2005.02.002

610 Pausas, J. G., & Bradstock, R. A. (2007). Fire persistence traits of plants along a productivity and
611 disturbance gradient in mediterranean shrublands of south-east Australia. *Global Ecology and*
612 *Biogeography*, 16(3), 330 – 340. https://doi.org/10.1111/j.1466-8238.2006.00283.x

613 Pausas, J. G., & Paula, S. (2012). Fuel shapes the fire–climate relationship: evidence from
614 Mediterranean ecosystems. *Global Ecology and Biogeography*, 21(11), 1074 – 1082.
615 https://doi.org/10.1111/j.1466-8238.2012.00769.x

616 Pausas, J. G., & Ribeiro, E. (2013). The global fire–productivity relationship. *Global Ecology and*
617 *Biogeography*, 22(6), 728 – 736. https://doi.org/10.1111/geb.12043

618 Petschick, R. MacDiff 4.1. 2. Powder diffraction software (2000). Available from the author at
619 http://www.geol.uni-erlangen.de/html/software/Macdiff.html.

620 Pieńkowski, G., Uchman, A., Ninard, K., & Hesselbo, S. P. (2021). Ichnology, sedimentology, and
621 orbital cycles in the hemipelagic Early Jurassic Laurasian Seaway (Pliensbachian, Cardigan Bay
622 Basin, UK). *Global and Planetary Change*, 207, 103648.
623 https://doi.org/10.1016/j.gloplacha.2021.103648

624 Rees, P. M., Ziegler, A. M. & Valdes, P. J. (2000). Jurassic phytogeography and climates: new data
625 and model comparisons. In Huber, B. T., Macleod, K. G. & Wing, S. L. (Eds.), *Warm Climates in*
626 *Earth History*. (pp. 297 – 318). Cambridge: Cambridge University Press.

627 Retallack, G. J. (2001). A 300-million-year record of atmospheric carbon dioxide from fossil plant
628 cuticles. *Nature*, 411(6835), 287 – 290. https://doi.org/10.1038/35077041

629 Riding, J. B., Leng, M. J., Kender, S., Hesselbo, S. P., & Feist-Burkhardt, S. (2013). Isotopic and
630 palynological evidence for a new Early Jurassic environmental perturbation. *Palaeogeography,*
631 *Palaeoclimatology, Palaeoecology*, 374, 16 – 27. https://doi.org/10.1016/j.palaeo.2012.10.019

632 Ruffell, A., McKinley, J. M. & Worden, R. H. (2002). Comparison of clay mineral stratigraphy to
633 other proxy palaeoclimate indicators in the Mesozoic of NW Europe. *Philosophical Transactions of*
634 *the Royal Society London A: Mathematical, Physical and Engineering Sciences*, 360, 675 – 693.
635 https://doi.org/10.1098/rsta.2001.0961

636 Ruhl, M., Hesselbo, S. P., Hinnov, L., Jenkyns, H. C., Xu, W., Riding, J. B., et al. (2016).
637 Astronomical constraints on the duration of the Early Jurassic Pliensbachian Stage and global climatic

fluctuations. *Earth and Planetary Science Letters*, 455, 149 – 165.

https://doi.org/10.1016/j.epsl.2016.08.038

Sellwood, B. W., & Valdes, P. J. (2008). Jurassic climates. *Proceedings of the Geologists'*
Association, 119(1), 5 – 17. https://doi.org/10.1016/S0016-7878(59)80068-7

Silva, R. L., Duarte, L. V., Wach, G. D., Ruhl, M., Sadki, D., Gómez, J. J. et al. (2021). An Early
Jurassic (Sinemurian–Toarcian) stratigraphic framework for the occurrence of organic matter
preservation intervals (OMPIs). *Earth-Science Reviews*, 221, 103780.

Steinthorsdottir, M., & Vajda, V. (2015). Early Jurassic (late Pliensbachian) CO2 concentrations
based on stomatal analysis of fossil conifer leaves from eastern Australia. *Gondwana Research*, 27(3),
932 – 939. https://doi.org/10.1016/j.gr.2013.08.021

Storm, M. S., Hesselbo, S. P., Jenkyns, H. C., Ruhl, M., Ullmann, C. V., Xu, W., et al. (2020). Orbital
pacing and secular evolution of the Early Jurassic carbon cycle. *Proceedings of the National Academy*
of Sciences, 117(8), 3974 – 3982. https://doi.org/10.1073/pnas.1912094117

Torsvik, T. H., & Cocks, L. R. M. (2017). Jurassic. In *Earth History and Palaeogeography*.
Cambridge: Cambridge University Press.

Trenberth, K. E., Fasullo, J., & Smith, L. (2005). Trends and variability in column-integrated
atmospheric water vapor. *Climate dynamics*, 24(7), 741 – 758. https://doi.org/10.1007/s00382-005-
0017-4

Ullmann, C. V., Szücs, D., Jiang, M., Hudson, A. J., & Hesselbo, S. P. (2022). Geochemistry of
macrofossil, bulk rock and secondary calcite in the Early Jurassic strata of the Llanbedr (Mochras
Farm) drill core, Cardigan Bay Basin, Wales, UK. *Journal of the Geological Society*, 179(1).
https://doi.org/10.1144/jgs2021-018

van de Schootbrugge, B., Bailey, T. R., Rosenthal, Y., Katz, M. E., Wright, J. D., Miller, K. G., et al.
(2005). Early Jurassic climate change and the radiation of organic-walled phytoplankton in the Tethys
Ocean. *Paleobiology*, 31(1), 73 – 97. https://doi.org/10.1666/0094-
8373(2005)031<0073:EJCCAT>2.0.CO;2

van der Werf, G. R., Randerson, J. T., Giglio, L., Collatz, G. J., Kasibhatla, P. S., & Arellano Jr, A. F.
(2006). Interannual variability in global biomass burning emissions from 1997 to 2004. *Atmospheric*
Chemistry and Physics, 6(11), 3423 – 3441. https://doi.org/10.5194/acp-6-3423-2006